Chemical Science

ROYAL SOCIETY OF CHEMISTRY

EDGE ARTICLE

View Article Online
View Journal | View Issue

Cite this: *Chem. Sci.*, 2026, **17**, 516

All publication charges for this article have been paid for by the Royal Society of Chemistry

Received 23rd September 2025
Accepted 2nd November 2025

DOI: 10.1039/d5sc07373a

rsc.li/chemical-science

Engineering O–O formation on dual-atom Fe–Mo catalysts for oxygen electrocatalysis

Luoluo Qi,[a] Yanan Tang,[*b] Tao Gan*[c] and Jingqi Guan[*a]

Although single-atom Fe–N–C catalysts exhibit outstanding oxygen reduction reaction (ORR) activity, their stability presents challenges due to the oxidation and destruction of Fe–N_x active sites by Fenton-like reactions, severely restricting their application in energy storage and conversion technologies. Here, we construct a dual-atom oxygen electrocatalyst (FeMo/NC) with $FeMoN_7$ active sites, which demonstrates excellent bifunctional oxygen electrocatalysis performance. The FeMo/NC-based zinc–air battery (ZAB) can operate continuously for over 200 h without significant activity decay, making it superior to the Fe/NC-based ZAB. *In situ* X-ray absorption spectroscopy (XAS) and Raman characterizations reveal the formation of the *Fe–O–O–Mo* intermediate with an oxygen bridge bond, which synergistically enables adsorption or desorption of O_2 through the Fe–Mo dual-atom sites, avoiding the limitations of the linear scaling relationship and thereby accelerating the oxygen electrocatalysis process. Density functional theory calculations reveal that the bridged oxygen adsorption mode on the Fe–Mo dual-atom sites exhibits lower energy barriers compared to that on single Fe/Mo sites, favoring the oxygen electrocatalysis.

Introduction

Oxygen electrocatalysis is crucial for green energy conversion and storage devices, for instance, zinc–air batteries (ZABs).[1,2] The kinetic bottleneck of reversible oxygen electrocatalysis constrains the energy conversion,[3,4] which directly determines the efficiency and practicality of these devices.[5,6] Single-atom catalysts (SACs) have been extensively explored to promote energy efficiency, especially Fe–N–C SACs with intrinsic activity for oxygen catalysis.[7,8] However, there is an as yet unresolved issue with SACs. In electrocatalytic reactions, the activation energy of reaction intermediates adsorbed on SACs exhibits a linear relationship.[9,10] Multiple reaction intermediates cannot simultaneously and stably coexist, which leads to the single functionality of SACs and makes it difficult to break through the linear relationship to achieve bifunctional oxygen catalysis.[9,11,12] In practice, dual-atom sites are constructed by adding additional sites to single-atom catalytic systems. By leveraging the synergistic effect of dual-atom sites, the limitation of the proportion relationship can be broken, allowing the adsorbed intermediates to adjust according to the changes in the reaction conditions, thereby realizing the transcendence of the intrinsic capabilities of SACs.[13,14]

For Fe-based SACs with Fe–N_x sites, structural stability is the centerpiece for maintaining their reversible oxygen catalysis activity.[15] During the reversible cycling of the oxygen electrocatalysis reaction, the Fe sites must maintain a dynamically stable coordination configuration and chemical state to avoid irreversible deactivation of the active sites due to oxidation, agglomeration or desorption.[16,17] Fe atoms with the electronic structure of $3d^6 4s^2$ readily experience chemical state transitions between +2 and +3 in an electrochemical environment. Alternatively, the deactivation of Fe–N_x sites can be accounted for by a variety of reasons, such as protonation of N groups, demetallization and carbon oxidation at different potentials in oxygen electrocatalysis.[18,19] Additionally, the Fe–N_x sites of Fe–N–C SACs are prone to participate in Fenton reactions, which release active $OH^{\bullet}$ and $OOH^{\bullet}$ radicals, causing the Fe–N bond to be broken or the carbon carrier to be oxidized, resulting in structural collapse, exposure and dissolution of the metal sites, and even the presence of numerous surface oxygen atoms, and resulting in an "oxygen-rich and iron-poor" situation.[20,21] Liu *et al.* utilized a defect trapping strategy to stabilize dual-atom Fe–Mn on a carbon-based material. $FeMn_{DSA}$/dNC presented outstanding ORR performance, with a half-wave potential ($E_{1/2}$) of 0.921 V, high peak power density of up to 291 mW cm^{-2} and remarkable durability (500 h at 5 mA cm^{-2}) in a ZAB.[22] Defective coordination of neighboring Fe–Mn dual-atom sites triggered charge redistribution and enhanced the d–p orbital hybridization between the Fe active sites and O atoms, which optimized the adsorption behavior of intermediates and enhanced the ORR kinetics. Wang *et al.* constructed a FeNi-NPC dual-atom catalyst (DAC) by anchoring dual-atom Fe and Ni in an N,P-

[a]*Institute of Physical Chemistry, College of Chemistry, Jilin University, 2519 Jiefang Road, Changchun 130021, P. R. China. E-mail: guanjq@jlu.edu.cn*

[b]*College of Physics and Electronic Engineering, Zhengzhou Normal University, Zhengzhou 450044, China. E-mail: yntang2010@163.com*

[c]*Shanghai Synchrotron Radiation Facility, Shanghai Advanced Research Institute, Chinese Academy of Sciences, Shanghai, 201204, China. E-mail: gant@sari.ac.cn*

codoped carbon substrate. The ZAB assembled with FeNi-NPC can run for 150 h at 3 mA cm^{-2}.[23] The electronic synergy of the Fe–Ni dimers and N and P heteroatoms enhanced the oxygen catalysis activity. These reports improved the stability of the Fe sites through the synergistic action of the dual-atom sites and surface modification strategies. However, during the electrocatalytic process, the catalyst structure is no longer the one obtained from the pre-preparation, but instead undergoes structural reconfiguration under the influence of the potential and electrolyte. Despite this, there are few works analyzing the coordination structure and chemical state of Fe sites after reconfiguration to confirm the stability of the Fe sites during oxygen electrocatalysis. Meanwhile, due to the electronic properties of the element Mo, it exhibits flexible valence state changes, that is, it can flexibly receive or give electrons, and thereby has a certain electronic modulation effect that can improve the microstructure of the main sites and enhance stability.[24,25] Therefore, the element Mo was selected for use in auxiliary sites to exert a synergistic mechanism with the Fe sites.

Here, we successfully fabricated a FeMo/NC DAC *via* a combination strategy of etching, targeted adsorption and activation. The FeMo/NC exhibits exceptional bifunctional oxygen catalytic performance. When assembled in the cathode of a ZAB, it demonstrates satisfactory performance with excellent durability for over 200 h (10 mA cm^{-2}), significantly outperforming ZABs assembled using Fe/NC SAC and commercial Pt/C + RuO_2. *In situ* XAS characterization reveals significant changes in the chemical state and coordination environment of the Fe/Mo sites and the formation of the *Fe–O–O–Mo* intermediate with an oxygen bridge configuration during the ORR/OER, while *in situ* Raman identifies the *O–O* intermediate adsorbed on the Fe–Mo sites. Further combining these results with DFT calculations indicates that the Fe atom interacts with Mo atom in the Fe–Mo dimer structure to establish the *Fe–O–O–Mo* mode, accomplishing O_2 adsorption, activation and desorption, and is superior to single Fe/Mo sites.

Experimental

Preparation of Fe/NC

$Zn(NO_3)_2 \cdot 6H_2O$ (1.594 g) and $Fe_2(SO_4)_3$ (0.054 g) were dissolved in methanol (80 mL) to form a homogeneous solution, while 2-methylimidazole (3.7 g) was also dissolved in methanol (80 mL) to form a homogeneous solution. The two solutions were then mixed and stirred for 24 h, and finally centrifuged, washed and dried to obtain a light-yellow powder, which was named ZnFe/ZIF. Next, ZnFe/ZIF was placed in a porcelain boat for calcination in a tube furnace, followed by calcination at 900 °C for 3 h under an N_2 atmosphere to obtain a black powder, which is denoted as Fe/NC.

Preparation of etched-Fe/NC

The Fe/NC (100 mg) was ultrasonically dispersed in a mixture of water (25 mL) and ethanol (25 mL). After 1 h, H_2O_2 (0.6 mL) was added to the solution. The mixture was stirred for 30 min and then placed in a Teflon-lined autoclave for reaction (110 °C, 3 h). After cooling to room temperature, the mixed solution was centrifuged, washed and dried to obtain etched-Fe/NC.

Preparation of FeMo/NC

The etched-Fe/NC (50 mg) was uniformly dispersed in a mixture of water (25 mL) and ethanol (25 mL) by sonication for 1 h. Then, $MoCl_3$ (1 mL, 10 mmol L^{-1}) was added to the mixed solution. After 2 h of stirring, the mixture was centrifuged, washed and dried to obtain the intermediate. Melamine and the intermediate were placed in upstream and downstream porcelain boats in a tube furnace for calcination at 900 °C for 1 h under the protection of N_2 to obtain the target product, which is denoted as FeMn/NC. Based on the mole content of $MoCl_3$, the products were named FeMo/NC-x (x = 0.005, 0.01 and 0.02 mmol). Additionally, Mo/NC was prepared *via* the same process as FeMo/NC without the addition of $Fe_2(SO_4)_3$.

Results and discussion

Synthesis and characterization

As shown in Fig. 1a, the oriented design of the dual-atom Fe–Mo sites can be achieved *via* a three-step procedure. Firstly, a single-atom Fe catalyst was obtained through high-temperature pyrolysis of FeZn–ZIF, vacancies were then formed near the Fe sites *via* H_2O_2 etching, and finally, dual-atom Fe–Mo sites were formed by adsorption and immobilization of Mo ions at the vacancies.[26,27] X-ray powder diffraction (XRD) patterns show only the diffraction peaks of the mesoporous carbon skeleton (JCPDS: 41-1487, 2H-Graphite) formed after the pyrolysis of ZIF, without any diffraction peaks due to metal nanoparticles or clusters, which indicates the good dispersion of Fe and Mo (Fig. S1).[28] The transmission electron microscopy (TEM) images in Fig. 1b and c demonstrate the morphology of the mesoporous carbon nanoframe of FeMo/NC without the presence of observable metal particles or clusters. Energy dispersive spectrometry (EDS) mapping images reveal that the elements C, N, Fe and Mo are evenly dispersed across the carbon skeleton (Fig. 1d, e and S2).[29] Moreover, aberration-corrected high-angle annular dark-field scanning transmission electron microscopy (AC-HAADF-STEM) images further corroborate the atomic dispersion of FeMo/NC. As depicted in Fig. 1f, the presence of numerous bright diffraction spots indicates the homogeneous distribution of Fe and Mo atoms in the substrate. Numerous paired diffraction bright spots are evident and have been indicated with red rectangles in Fig. 1g, showing the successful construction of Fe–Mo dual-atom sites.[30] In particular, the 3D atomic overlap maps corresponding to the dimers in the white circles are favorable evidence for the formation of dual-atom Fe–Mo sites (Fig. 1h). Additionally, Fig. 1i presents the intensity distribution of the paired diffracted bright spots in Fig. 1g, where the distance between Fe and Mo atoms is about 0.273 nm.

The chemical states of all elements in the FeMo/NC catalyst were studied using X-ray photoelectron spectroscopy (XPS). The presence of the elements C, N, O, Fe and Mo in FeMo/NC is shown in the XPS survey spectrum (Fig. S3a). As indicated in Fig. S3b, the high-resolution Fe 2p spectrum of FeMo/NC is divided into two regions, corresponding to the Fe $2p_{1/2}$ and Fe

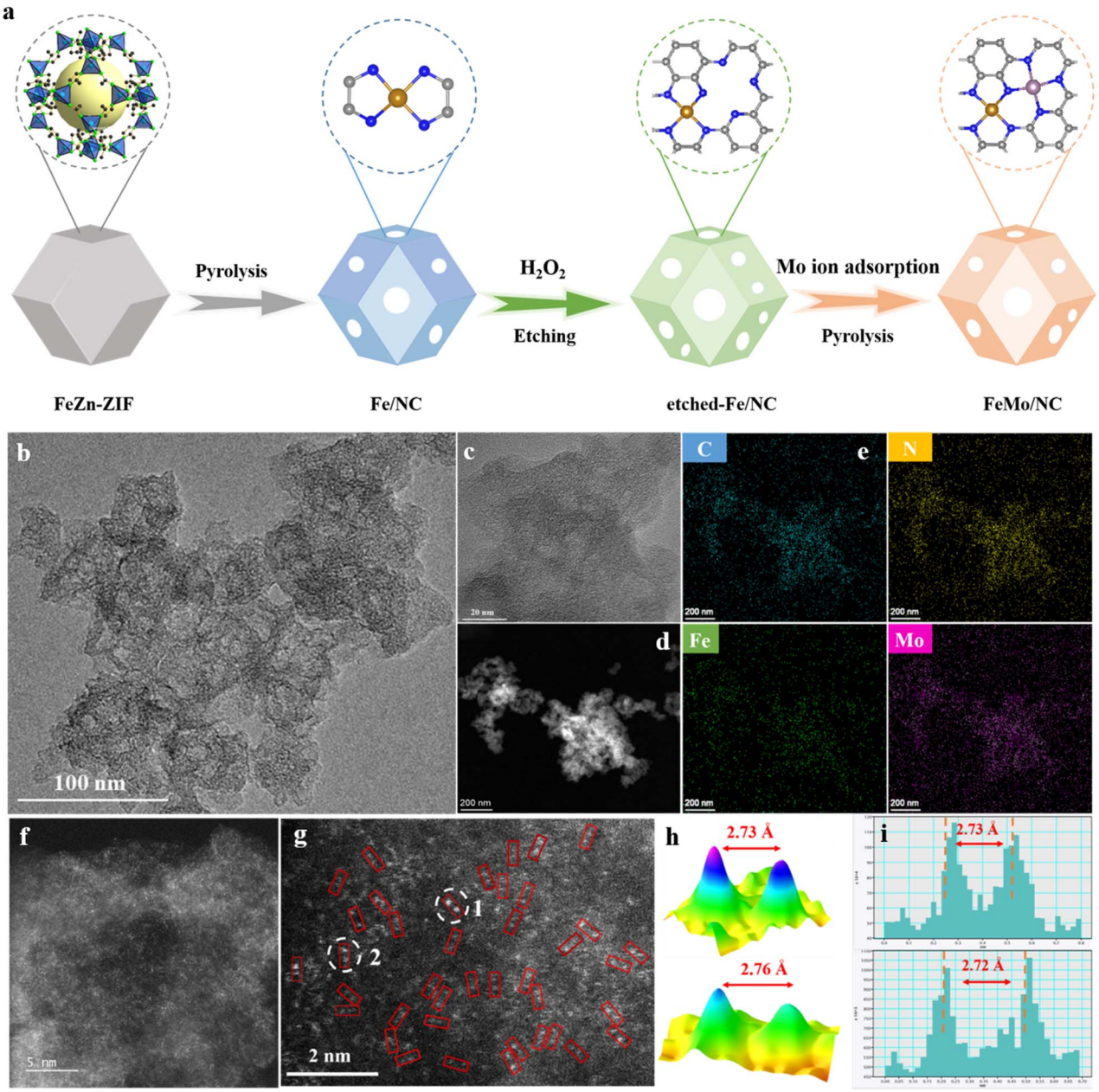

Fig. 1 (a) Synthesis process, (b and c) HR-TEM images, (d and e) HAADF-STEM image and EDS elemental mapping images, and (f and g) AC-STEM images of FeMo/NC. (h) 3D diagram of the atomic arrangement and (i) distance estimation for the Fe–Mo dimers of FeMo/NC.

$2p_{3/2}$ peaks at 723.4 eV and 713 eV, respectively, which are both attributed to the Fe–N_x moiety.[31,32] Importantly, the two peaks of Fe 2p in FeMo/NC are negatively shifted relative to that of Fe/NC, suggesting a lower oxidation state of Fe in FeMo/NC due to partial charge sharing with the introduction of Mo. Additionally, the high-resolution Mo 3d spectrum was deconvoluted into two peaks at 228.2 eV and 232.2 eV, which correspond to the $3d_{5/2}$ and $3d_{3/2}$ orbitals (Fig. S3c).[33] The high-resolution N 1s spectrum in FeMo/NC presents four major peaks attributed to pyridinic-N (398.7 eV), Fe–N/Mo–N (399.8 eV), pyrrolic-N (400.8 eV) and graphitic-N (401.9 eV) (Fig. S3d).[34,35] Compared to that of Fe/NC, the relative content of pyridinic-N in FeMo/NC is significantly increased due to the disappearance of the *N*-oxide peak, which is strongly responsible for the enhancement of the ORR activity.[36,37] Further, the chemical state and local coordination environment of the Fe–Mo dual-atom sites in FeMo/NC were verified using XAS. As shown in Fig. 2a, with reference to Fe foil, FeO and Fe_2O_3, the X-ray absorption near-edge structure (XANES) of Fe is located between those of FeO and Fe_2O_3, suggesting that the oxidation state of Fe is between +2 and +3. Analogously, the oxidation state of Mo is about +6 (Fig. 2b). As indicated in Fig. 2c–f and Table S1, the bond length of Fe–N coordination is 1.980 ± 0.016 Å in the first shell according to Fe K-edge Fourier-transform EXAFS (FT-EXAFS). The distance of Fe–Mo scattering path is 3.698 ± 0.015 Å, which can be distinguished from the Fe–Fe scattering (2.2 Å) in Fe foil and Fe–O–Fe scattering (2.55 Å) in Fe_2O_3. Likewise, the two

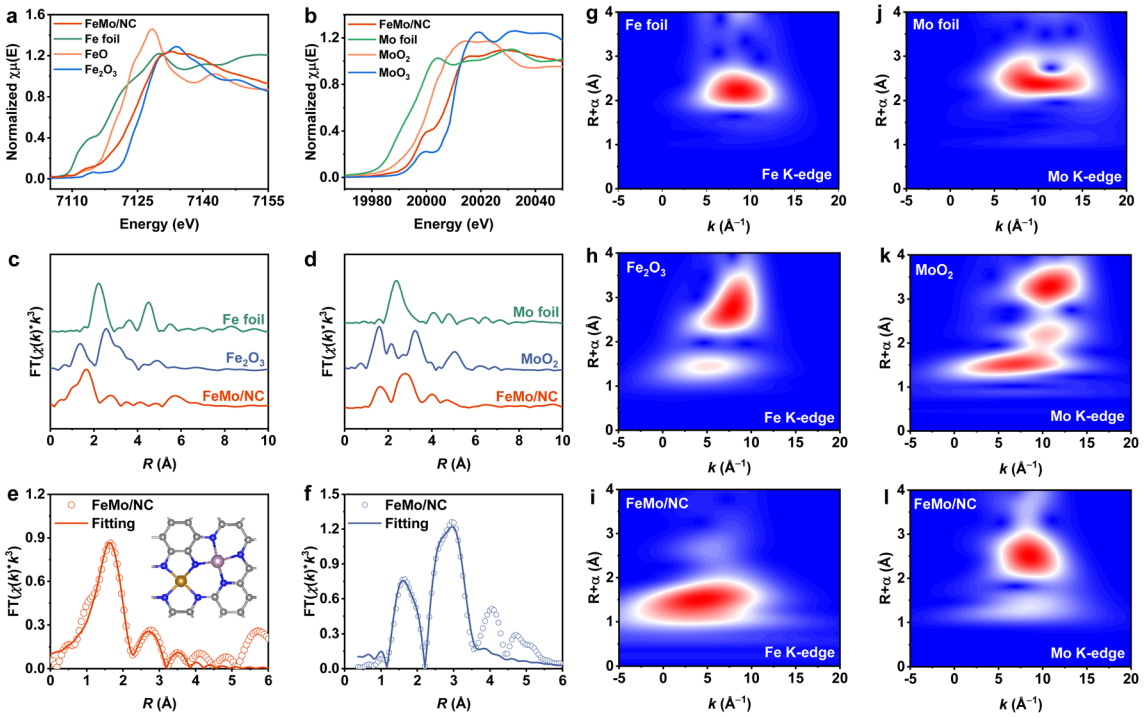

Fig. 2 (a) Fe K-edge and (b) Mo K-edge XANES spectra. (c) Fe K-edge and (d) Mo K-edge FT-EXAFS spectra. FT-EXAFS fitting spectra at the (e) Fe K-edge (inset: the simulated structure) and (f) Mo K-edge. Fe K-edge WT-EXAFS spectra of (g) Fe foil, (h) Fe_2O_3 and (i) FeMo/NC. Mo K-edge WT-EXAFS spectra of (j) Mo foil, (k) MoO_2 and (l) FeMo/NC.

dominant peaks at 2.100 ± 0.012 Å and 3.704 ± 0.017 Å in the Mo K-edge FT-EXAFS correspond to Mo–N and Mo–Fe scattering paths, respectively. The average coordination numbers of Fe–N, Fe–Mo, Mo–N and Mo–Fe are 3.80 ± 0.18, 1.00 ± 0.13, 4.20 ± 0.20 and 1.20 ± 0.17, respectively. Therefore, according to the fitting results, the Fe–Mo dual-atom sites of FeMo/NC can be rationally constructed as $FeMoN_7$ with the Fe atom bridged to the Mo atom by a nitrogen atom (inset in Fig. 2e). Additionally, wavelet-transform EXAFS (WT-EXAFS) spectra were plotted to perceptually depict the coordination environment. As depicted in Fig. 2g–l, the *k*-values at ~4.0 $Å^{-1}$ and ~5.0 $Å^{-1}$ are consistent with Fe–N coordination and Fe–Mo coordination, respectively, while the two scattering paths with *k*-values at ~8.4 $Å^{-1}$ and ~8.7 $Å^{-1}$ correspond to Mo–N and Mo–Fe coordination. Obviously, the absence of signals from Fe–Fe and Mo–Mo scattering paths confirms the dual-atom coordination structure of the Fe, Mo and N atoms.

Oxygen electrocatalysis performance

The catalytic activity of FeMo/NC and the comparison catalysts Fe/NC, Mo/NC and Pt/C in the ORR was investigated in 0.1 M KOH. By modulating the concentration of Mo during the synthesis process, it was found that FeMo/NC exhibits the optimal catalytic performance in the ORR when 0.01 mmol of Mo is introduced (Fig. S4 and S5). In the CV curves, FeMo/NC has the most positive cathodic reduction peak position, indicating its outstanding oxygen reduction advantage (Fig. S6).[20] Complementarily, as shown in Fig. 3a, FeMo/NC demonstrates a higher onset potential of 1.01 V and half-wave potential of 0.91 V compared to Fe/NC ($E_{onset} = 0.98$ V, $E_{1/2} = 0.88$ V), Mo/NC ($E_{onset} = 0.91$ V, $E_{1/2} = 0.81$ V) and Pt/C ($E_{onset} = 0.94$ V, $E_{1/2} = 0.84$ V), supporting the efficiency of the design for the incorporation of the second metal Mo into a single-atom Fe system to establish highly active Fe–Mo dual-atom sites.[38] Moreover, the limiting diffusion current density of FeMo/NC ($J_L = -5.34$ mA cm^{-2}) at 0.5 V_{RHE} is significantly higher than that of Fe/NC ($J_L = -4.47$ mA cm^{-2}), Mo/NC ($J_L = -2.47$ mA cm^{-2}) and Pt/C ($J_L = -5.22$ mA cm^{-2}). Moreover, FeMo/NC exhibits a high kinetic current density (J_k) of 44.7 mA cm^{-2}, which is about 4 times that of Fe/NC ($J_k = 12.6$ mA cm^{-2}) and 14 times that of Pt/C ($J_k = 3.2$ mA cm^{-2}), illustrating the high mass transfer efficiency and strong intrinsic catalytic ability of FeMo/NC (Fig. 3b). Simultaneously, the larger electrochemically active surface area of FeMo/NC (13.5 mF cm^{-2}) indicates more active sites for the oxygen electrocatalysis (Fig. S7). In Fig. 3c, FeMo/NC shows faster ORR kinetics with a Tafel slope of 53.8 mV dec^{-1}, which is favorable in comparison to that of Fe/NC (56.4 mV dec^{-1}), Mo/NC (86.2 mV dec^{-1}) and Pt/C (70.6 mV dec^{-1}).[39] Additionally, FeMo/NC displays superior ORR catalytic activity, surpassing that of most DACs (Table S2). The K–L plot was derived from the LSV curves of the series rotation speed and illustrated that FeMo/NC delivers a 4-electron-dominated ORR process (Fig. 3d).[40] Subsequently, RRDE testing further confirmed the desirable $4e^-$ pathway. As depicted in Fig. 3e, the electron transfer number (*n*) on FeMo/NC remains very close to 4 and the H_2O_2 yield remains below 6% at varying potentials, comparable to that of the benchmark catalyst Pt/C, once again reflecting the satisfactory ORR kinetics.[41] Furthermore, the ability of FeMo/NC to remain active over long periods of operation is a guarantee of its practical applicability. As

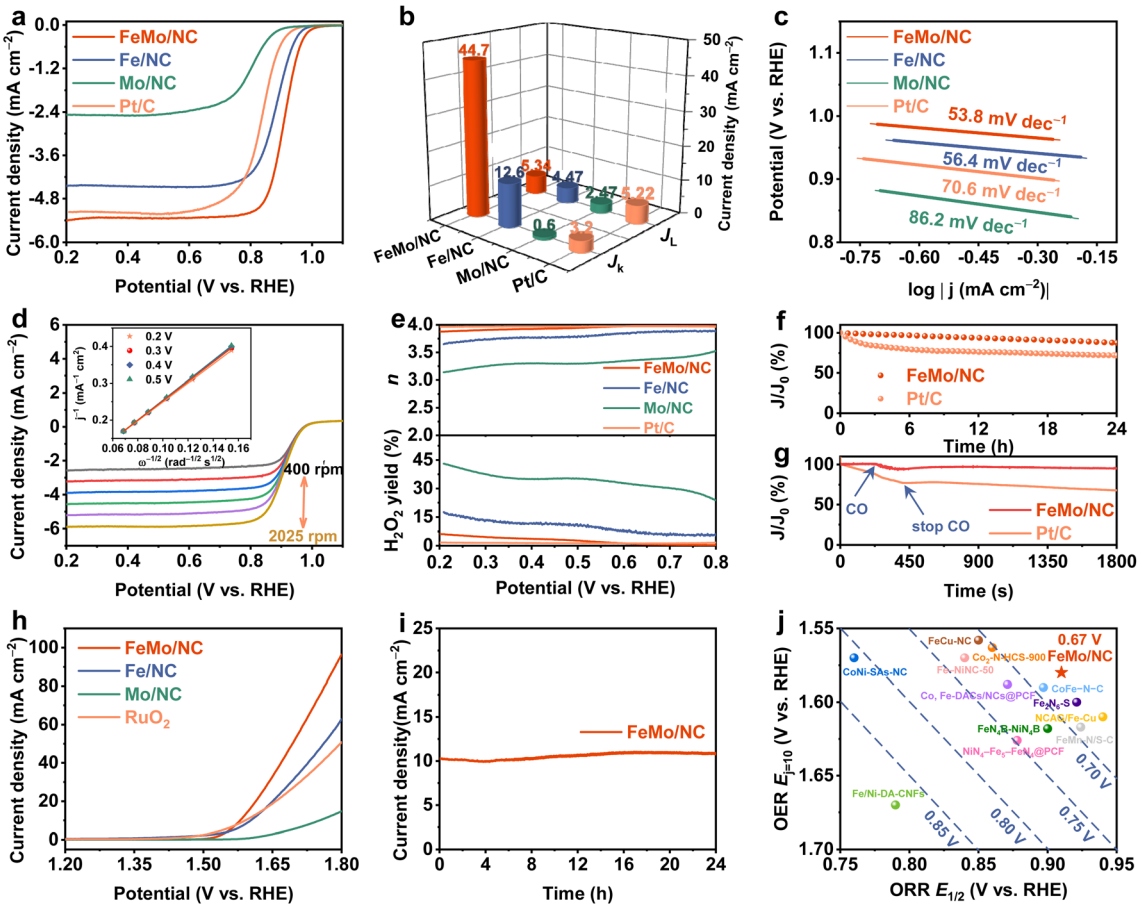

Fig. 3 (a) LSV polarization curves for the ORR. (b) Comparison of $E_{1/2}$ and J_K @ 0.85 V. (c) Tafel slopes. (d) LSV polarization curves of FeMo/NC at series rotation speed (inset: K–L plots). (e) H_2O_2 yield (%) and electron transfer number (n). (f) Stability tests and (g) corrosion resistance to CO on FeMo/NC and Pt/C. (h) LSV polarization curves for the OER. (i) Stability tests for FeMo/NC at 10 mA cm^{-2}. (j) Comparison of ΔE.

indicated in Fig. 3f, after 24 h of operation, FeMo/NC retains 88% of its initial activity, which is significantly better than the 72% activity retention rate of Pt/C, implying excellent durability of FeMo/NC in corrosive alkaline environments. Additionally, after CO is introduced into the solution, the current density of FeMo/NC shows only a small loss, with 95% retained relative to the initial value, whereas the current density of Pt/C drops significantly and shows essentially no recovery, illustrating the applicability of FeMo/NC (Fig. 3g). Additionally, FeMo/NC performs better than Pt/C in the methanol tolerance test (Fig. S8). Meaningfully, the KSCN poisoning test can fully demonstrate the stability of the Fe–Mo dual-atom active sites. After the addition of 10 mM KSCN, the E_{onset}, $E_{1/2}$ and J_L of FeMo/NC fluctuate very little, whereas the fluctuation of Pt/C is evident, indicating the effectiveness of the FeMo dual-atom coordination with N, which effectively prevents the loss of activity due to SCN^- adsorbed on Fe–Mo dual-atom sites (Fig. S9).[42]

The OER performance of FeMo/NC and the control catalysts, including Fe/NC, Mo/NC and RuO_2, was evaluated in 1.0 M KOH. As in the case of the ORR, the addition of 0.01 mmol Mo during the synthesis of FeMo/NC was found to be optimal for the OER (Fig. S10 and S11). As shown in Fig. 3h, FeMo/NC exhibits a lower overpotential (η_{10} = 350 mV) than Fe/NC (η_{10} = 373 mV), Mo/NC (η_{10} = 522 mV) and RuO_2 (η_{10} = 361 mV), demonstrating that the interaction between the Fe atoms and the introduced Mo promotes OER activity.[43] Additionally, compared to the reference catalysts, FeMo/NC exhibits faster reaction kinetics and electron transfer rates, a larger active surface area, and a lower OER energy barrier (Fig. S12). Furthermore, in the chronopotentiometry test, the current of FeMo/NC essentially remains steady, with a slight upward trend during long-term operation for 24 h (Fig. 3i), further illustrating the superiority of the synergistic coordination of FeMo dual-atom engineering.[44] The results of the oxygen electrocatalysis experiments describe the bifunctional properties of FeMo/NC, which can be estimated from the potential difference ($\Delta E = E_{1/2} - E_{j=10}$).[45] As demonstrated in Fig. 3j, S13 and Table S3, FeMo/NC showcases the smallest ΔE value (ΔE = 0.67 V), which is lower than those of the control catalysts and most reported DACs, suggesting that its oxygen electrocatalysis performance possesses the qualities for application in ZABs.

Study of the structural evolution during oxygen electrocatalysis

To better elucidate the structural evolution of the FeMo/NC during oxygen electrocatalysis, *in situ* XAS was employed to

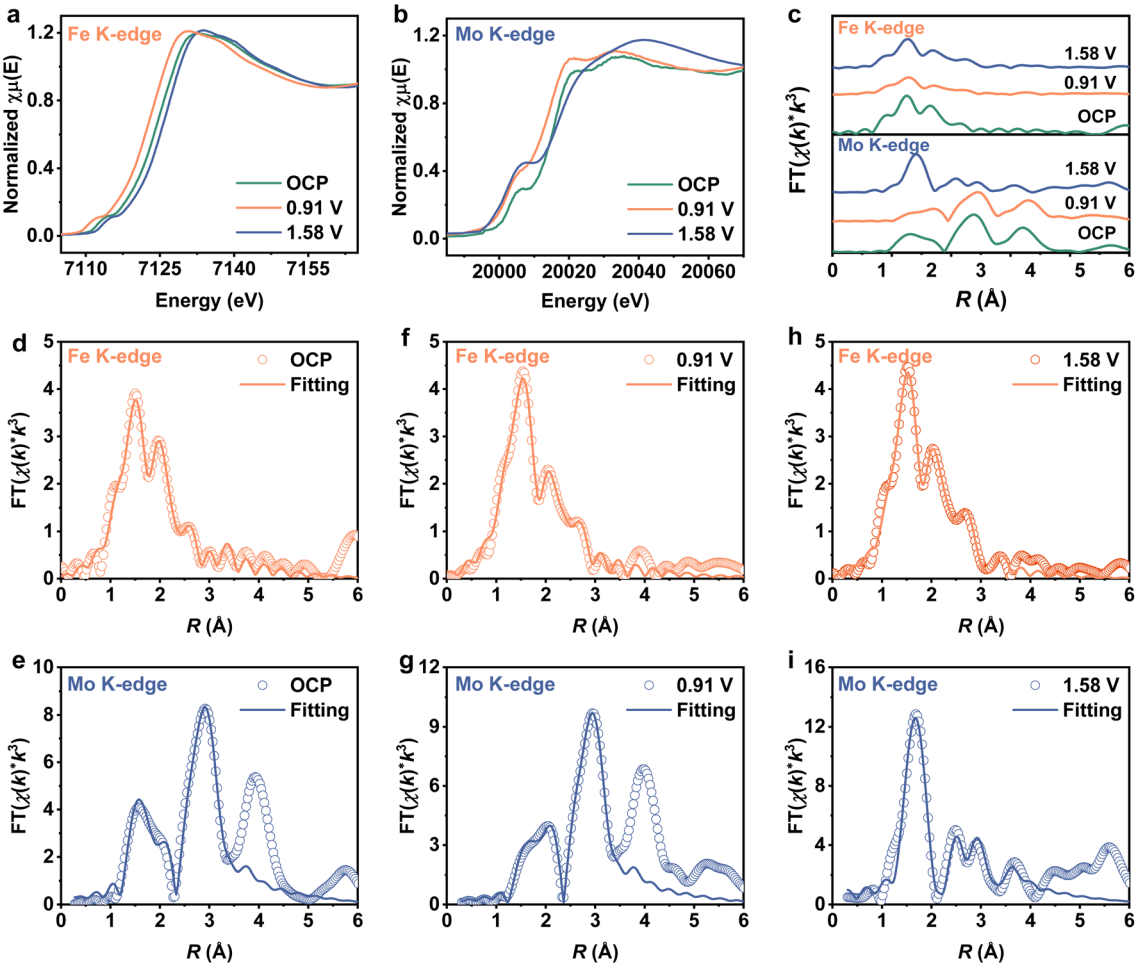

Fig. 4 *In situ* XAS of FeMo/NC at the OCP, 0.91 V and 1.58 V *vs.* RHE. (a) Fe K-edge and (b) Mo K-edge XANES spectra. (c) Fe K-edge and Mo K-edge FT-EXAFS spectra. FT-EXAFS fitting spectrum at the Fe K-edge and Mo K-edge of FeMo/NC (d and e) at the OCP, (f and g) at 0.91 V, and (h and i) at 1.58 V.

obtain the chemical state and local coordination features of the active sites in alkaline solution. As shown in Fig. 4a and b, compared to those at the open-circuit potential (OCP), the Fe K-edge and Mo K-edge XANES curves shift to lower and higher energy positions at 0.91 V and 1.58 V, respectively, which indicates that during the ORR and OER processes, both Fe and Mo sites are involved in the adsorption or desorption of oxygen-containing intermediates with electron transfer occurring, leading to different degrees of oxidation and reduction of Fe and Mo. Next, FT-EXAFS was used to detect the evolution of the Fe–Mo dual-atom sites during the oxygen electrocatalysis. In Fig. 4c, the shifts of the Fe–N, Fe–Mo, Mo–N and Mo–Fe peaks are obvious at 0.91 V and 1.58 V, which indicates that the adsorption of the intermediates at the Fe/Mo sites results in obvious stretching or contraction.[36] This suggests that during the OER and ORR processes, the Fe/Mo sites and the local coordination environment inevitably undergo charge rearrangement to regulate the adsorption and desorption of the intermediates. Moreover, the fitted FT-EXAFS curves reveal information on the coordination bonds and coordination numbers of the Fe–Mo dual-atom active sites (Fig. 4d–i and Table S4). The simultaneous occurrence of Fe–O and Mo–O coordination with coordination numbers of 0.9 and 1.1 at 0.9 V is ascribed to the adsorption of oxygen-containing species on the dual-atom sites in a bridge-on configuration to form the *Fe–O–O–Mo* intermediate and subsequent proton/electron transfer steps to produce the associated oxygen-related species.[46] Equivalently, the respective coordination numbers of 1.0 and 1.2 for Fe–O and Mo–O coordination at 1.58 V reflect the adsorption of *OH or *O species on the Fe/Mo sites, ultimately releasing O_2 in the *Fe–O–O–Mo* conformation. In addition, a slight increase in the coordination number of Fe–N, Mo–N, Fe–Mo, and Mo–Fe at 0.9 V and 1.58 V, related to the adsorption of oxygen-containing intermediates at the Fe–Mo dual-atom sites, suggests the predominance of $FeMoN_7$ in enabling the oxygen catalytic activity. Importantly, the *k*-value trends of the Fe–N, Fe–Mo, Mo–N, and Mo–Fe scattering paths in WT-EXAFS at 0.9 V and 1.58 V are consistent with those in FT-EXAFS, which are positively shifted, without the characteristic signals of Fe–Fe or Mo–Mo coordination, which suggests that $FeMoN_7$ maintains the local structure stability in the OER/ORR (Fig. S14). Therefore, based on the changes in oxidation state

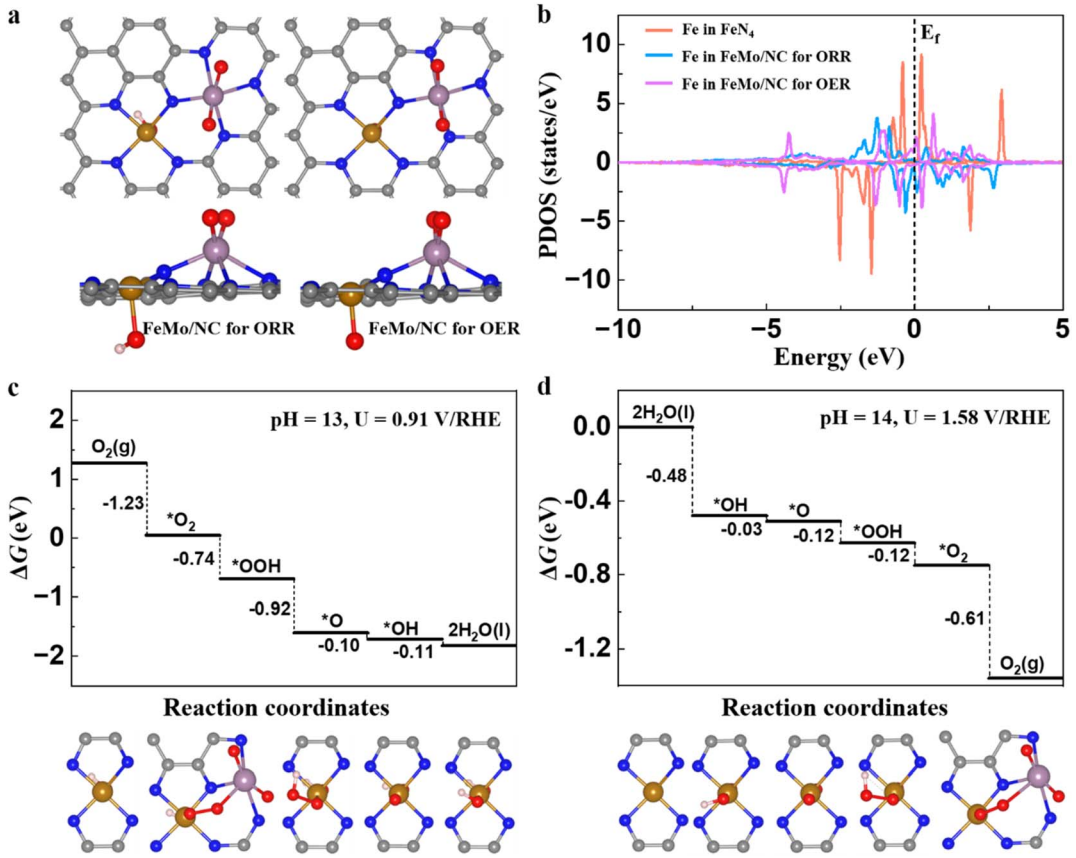

Fig. 5 (a) Top and side views of the atomic models of FeMo/NC for the ORR and OER. (b) Projected density of states (PDOS) of the Fe 3d orbitals for the FeN_4 SAC and for the Fe active center in FeMo/NC for the ORR and OER, respectively. Free energy diagrams and corresponding configurations of the reaction intermediates for the (c) ORR and (d) OER on the FeMo/NC catalyst.

and coordination information, it can be inferred that the Fe–Mo dual-atom site is a bifunctional active site for oxygen catalysis, where the Fe and Mo atoms synergistically form the key intermediate *Fe–O–O–Mo* to promote oxygen catalysis.

In situ Raman was further performed to detect the reaction intermediates at different ORR/OER potentials as well as to identify active sites in the reactions. As demonstrated in Fig. S15a, two peaks appear at ~1130 and ~1540 cm^{-1} when the potential changes (0.2–1.0 V). The peak located at ~1130 cm^{-1} arises from the O–O stretching vibration, which reflects the presence of the key intermediate *O–O*, suggesting that Fe and Mo atoms interact to form the *Fe–O–O–Mo* configuration during the ORR process.[47,48] The peak at ~1540 cm^{-1} corresponds to FeOOH species, which indicates the completion of the first step of ORR, that is, the conversion of *Fe–O–O–Mo* to FeOOH.[30] For the OER, the vibrations of Fe–OH and Fe–O appear at ~480 and ~790 cm^{-1}, respectively, while the peak around 1132 cm^{-1} belongs to the O–O stretching vibration in the *Fe–O–O–Mo* intermediate, reflecting the preferential activity of the Fe site and the synergistic role of the Mo site.[48] The peak at around 970 cm^{-1} is attributed to the O–H deformation vibration of the OH^- group (Fig. S15b).[44,49] Additionally, the I_D/I_G value rises with increasing OER potential, which indicates that the disorder of the material increases and more defects are created, providing more adsorption sites for the intermediates, thereby accelerating the OER kinetics. Thus, the combined *in situ* XAS and *in situ* Raman results demonstrate that the Fe–Mo dual-atom site is the effective active center for the OER/ORR, forming a bridged superoxide species.

Study of the oxygen electrocatalysis mechanisms

To elucidate the reaction pathways on the FeMo/NC catalyst, we investigated their surface states and constructed free energy profiles for both the ORR and OER using constant-potential first-principles calculations.[50,51] As a first step, we examined the possible pre-adsorption of O and OH species at the Mo and Fe centers under relevant electrochemical conditions. Taking an Fe, Mo co-embedded carbon nanoframe as the model as shown in Fig. S16, for the ORR at pH = 13 and U_{RHE} = 0.91 V, the Mo site tends to be occupied by two O atoms, while the Fe site is simultaneously coordinated by a single OH group. Notably, further adsorption of O or OH species at the Mo site leads to the cleavage of Mo–N bonds, indicating structural instability. Therefore, the catalytically active site for the ORR under these conditions is most likely the Fe center coordinated with one OH ligand, as illustrated in Fig. 5a. For the OER, under the relevant electrochemical conditions (pH = 14 and U_{RHE} = 1.58 V), a similar surface configuration is observed, with the

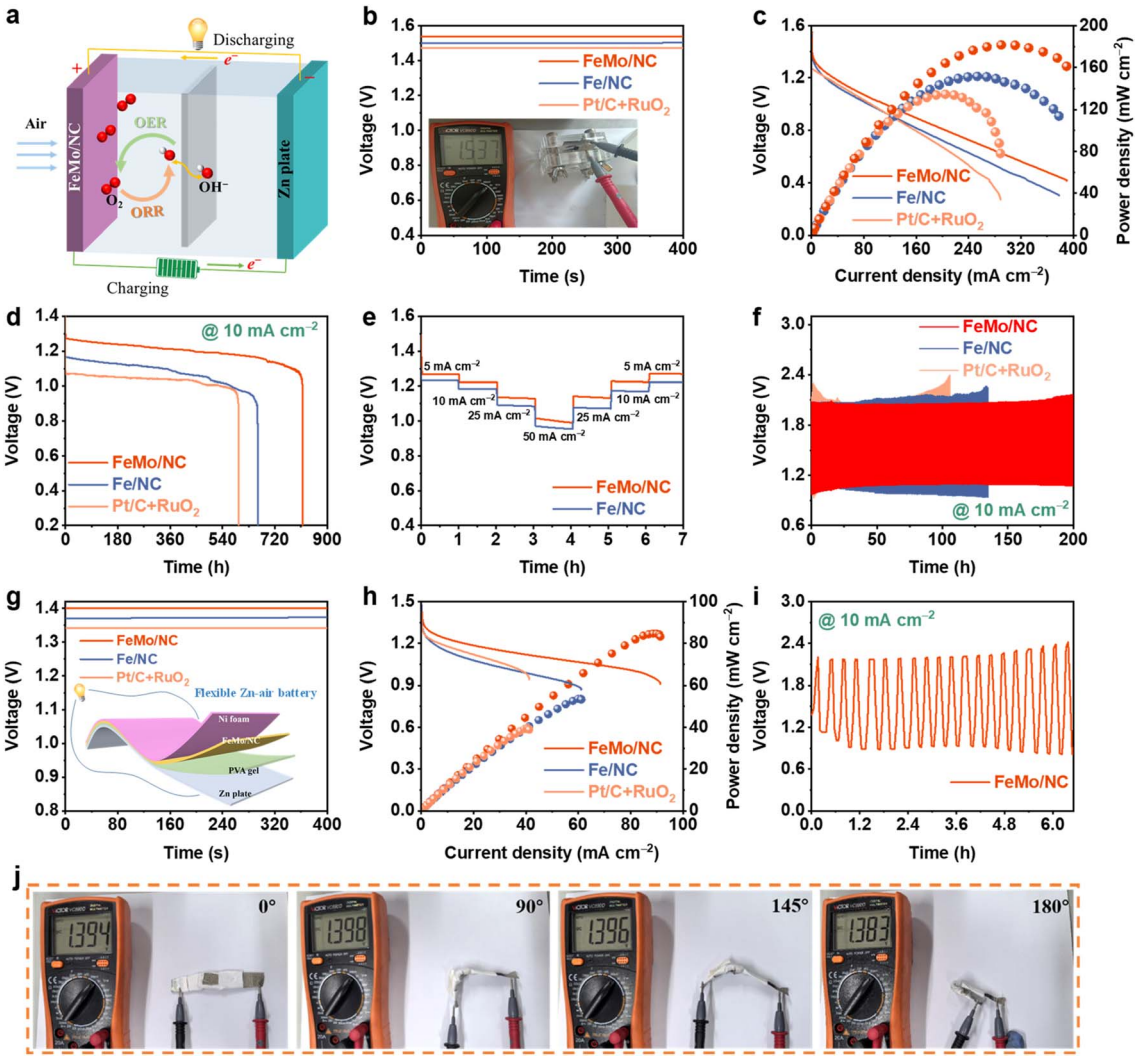

Fig. 6 (a) Device diagram of the liquid-ZAB with FeMo/NC as the air cathode. (b) OCV curves, (c) power density and discharge curves and (d) specific capacity of FeMo/NC-based, Fe/NC-based and Pt/C + RuO_2-based LZABs. (e) Voltage platforms of FeMo/NC-based and Fe/NC-based LZABs at a series of discharge densities. (f) Long-term durability of FeMo/NC-based, Fe/NC-based and Pt/C + RuO_2-based LZABs. (g) OCV (inset: schematic diagram of FZAB assembly) and (h) power density and discharge curves of FeMo/NC-based, Fe/NC-based and Pt/C + RuO_2-based FZABs. (i) Long-term durability of FeMo/NC-based FZAB. (j) OCV of FeMo/NC-based FZAB at different folding angles.

exception that the Fe site is instead coordinated by a single O atom (Fig. S17). This suggests that the active site for the OER is the Fe center bearing one O ligand (Fig. 5a).

We then investigated the electronic properties of the Fe active center. As shown in Fig. 5b, compared with the pristine FeN_4 SAC, the d states of the Fe center in FeMo/NC are significantly delocalized due to the presence of an axial ligand and neighboring Mo–O groups. This can optimize intermediate binding energies and thereby enhance both ORR and OER activity.[52] The free energy diagrams and corresponding intermediates for the ORR are presented in Fig. 5c. At pH = 13 and U_{RHE} = 0.91 V, all reaction steps are exothermic, consistent with the excellent ORR performance observed for FeMo/NC under these conditions. Similarly, for the OER at pH = 14 and U_{RHE} = 1.58 V, all steps are also exothermic (Fig. 5d), further supporting the high OER catalytic activity of this material. It can be observed that the adsorption or desorption of O_2 conforms to the *Fe–O–O–Mo* configuration during the ORR and OER, which is consistent with the *in situ* XAS and Raman experiments, confirming the synergistic oxygen catalytic mechanism of the Fe and Mo atoms. Together, these simulations provide strong theoretical support for the nature of the bifunctional active center that is behind the superior ORR/OER performance of the FeMo/NC catalyst.

Performance of FeMo/NC in Zn–air batteries

As the electrochemical experiments confirmed the excellent bifunctional oxygen catalytic performance of FeMo/NC, it was applied to the air cathode of a liquid zinc–air battery (LZAB) to evaluate its application potential (Fig. 6a). Additionally, a Fe/NC-based LZAB and Pt/C + RuO_2-based LZAB were assembled as comparisons. As displayed in Fig. 6b, the FeMo/NC-based

LZAB exhibits a high open-circuit voltage (OCV) of 1.54 V, which is superior to that of the Fe/NC-based LZAB (1.50 V) and the Pt/C + RuO_2-based LZAB (1.47 V). At the same time, the FeMo/NC-based LZAB provides a larger peak power density (181.6 mW cm^{-2}) and specific capacity (815.5 mAh g_{Zn}^{-1}) than the Fe/NC-based LZAB (151.5 mW cm^{-2}, 661.0 mAh g_{Zn}^{-1}) and Pt/C + RuO_2-based LZAB (134.7 mW cm^{-2}, 595.0 mAh g_{Zn}^{-1}) (Fig. 6c and d). Moreover, the performance of the FeMo/NC-based LZAB exceeds that of many published DACs (Table S5). Furthermore, as shown in Fig. 6e, the FeMo/NC-based LZAB demonstrates a stable voltage platform at varying current densities (5–50 mA cm^{-2}). The discharge voltage and voltage recovery performance both outperform those of the Fe/NC-based LZAB, reflecting the excellent discharge rate performance of the FeMo/NC-based LZAB.[53] Importantly, stability must be considered in addition to activity. As illustrated in Fig. 6f and S18, the FeMo/NC-based LZAB can operate steadily for 200 h at 10 mA cm^{-2}, with only a small difference between the initial and final energy efficiency and voltage gap. In contrast, the Fe/NC-based LZAB and the Pt/C + RuO_2-based LZAB show significant increases in the voltage gap and marked decreases in energy efficiency after a short period of operation. These results reinforce the advantages of the Fe–Mo synergism in FeMo/NC and highlight its potential for applications requiring ultra-long device lifetimes. Moreover, the FeMo/NC-based LZAB still performs much better than the Fe/NC-based LZAB in stability tests at a higher current density (20 mA cm^{-2}) (Fig. S19). Furthermore, a flexible zinc–air battery (FZAB) based on FeMo/NC as the cathode exhibited an OCV of 1.40 V and a peak power density of 84.7 mW cm^{-2}, which were superior to those of the Fe/NC-based FZAB and Pt/C + RuO_2-based FZAB (Fig. 6g and h). As shown in Fig. 6i, the charge/discharge stability at 10 mA cm^{-2} of the Fe/NC-based FZAB can be sustained for up to 6 h. When the degree of bending of the FeMo/NC-based FZAB is varied, its open-circuit voltage remains essentially stable, suggesting stability and robust flexibility (Fig. 6j).

Conclusions

The controllable synthesis of an FeMo/NC DAC has been realized by an integrated strategy involving the etching of a Fe-SAC, Mo ion adsorption, and high-temperature activation. XAS and HAADF-STEM characterizations demonstrate a dimer structure of FeMo/NC with the configuration $FeMoN_7$, in which the Fe and Mo atoms are bridged by an N atom. FeMo/NC exhibits excellent oxygen catalytic activity and stability, accompanied by a high $E_{1/2}$ of 0.91 V and low OER overpotential of 350 mV. Moreover, FeMo/NC shows superior performance in both LZABs and FZABs, demonstrating an outstanding OCV (1.54 and 1.40 V), high power density (181.6 and 84.7 mW cm^{-2}), and excellent stability and flexibility, indicating that it possesses potential for future applications. *In situ* XAS and Raman experiments demonstrated that the Fe atom couples with Mo atoms to form a *Fe–O–O–Mo* intermediate for the conversion of oxygen species during the processes, which is a more kinetically favorable pathway for the ORR/OER. DFT calculations confirmed lower energy barriers on the dual-atom Fe–Mo sites than single-atom Fe/Mo sites for the ORR/OER due to the concerted catalysis between Fe and Mo atoms. Thus, this work provides a unique demonstration of the structural evolution and reaction mechanism of the Fe–Mo DAC in oxygen electrocatalysis in terms of *in situ* experiments and theoretical calculations.

Author contributions

L. L. Q.: data curation, investigation, writing – original draft. Y. N. T.: investigation. T. G.: investigation. J. Q. G.: conceptualization, supervision, writing – review and editing.

Conflicts of interest

There are no conflicts to declare.

Data availability

The data supporting this article have been included as part of the supplementary information (SI). Supplementary information: additional experimental details on material characterization, electrochemical evaluation, Zn–air battery test, DFT methods, experimental data analysis methods, Fig. S1–S19 and Tables S1–S5. See DOI: **https://doi.org/10.1039/d5sc07373a**.

Acknowledgements

This work was supported by the National Natural Science Foundation of China (No. 22075099), and the Innovative Research Team (in Science and Technology) in University of Henan Province (Grant No. 25IRTSTHN015). The authors thank BL11B beamline (31124.02.SSRF.BL11B) of the Shanghai Synchrotron Radiation Facility for providing the XAS beamtime.

References

1 M. Xiao, J. Zhu, S. Li, G. Li, W. Liu, Y.-P. Deng, Z. Bai, L. Ma, M. Feng, T. Wu, D. Su, J. Lu, A. Yu and Z. Chen, *ACS Catal.*, 2021, **11**, 8837–8846.
2 J. Zhu, M. Xiao, G. Li, S. Li, J. Zhang, G. Liu, L. Ma, T. Wu, J. Lu, A. Yu, D. Su, H. Jin, S. Wang and Z. Chen, *Adv. Energy Mater.*, 2019, **10**, 1903003.
3 C. Chen, Z. Tang, J. Li, C. Du, T. Ouyang, K. Xiao and Z. Liu, *Adv. Funct. Mater.*, 2022, **33**, 2210143.
4 T. Bao, Y. Wu, C. Tang, Y. Xi, Y. Zou, P. Shan, C. Zhang, W. Drożdż, A. R. Stefankiewicz, P. Yuan, C. Yu and C. Liu, *Adv. Mater.*, 2025, **37**, 2500399.
5 L. Lei, X. Guo, X. Han, L. Fei, X. Guo and D. G. Wang, *Adv. Mater.*, 2024, **36**, 2311434.
6 G. Li, X. Wang, J. Fu, J. Li, M. G. Park, Y. Zhang, G. Lui and Z. Chen, *Angew. Chem., Int. Ed.*, 2016, **55**, 4977–4982.
7 M. Xiao, Z. Xing, Z. Jin, C. Liu, J. Ge, J. Zhu, Y. Wang, X. Zhao and Z. Chen, *Adv. Mater.*, 2020, **32**, 2004900.
8 Z. Zhang, J. Sun, F. Wang and L. Dai, *Angew. Chem., Int. Ed.*, 2018, **57**, 9038–9043.

9 P. Zhu, X. Xiong, D. S. Wang and Y. D. Li, *Adv. Energy Mater.*, 2023, **13**, 2300884.
10 W. Zhang, Y. Chao, W. Zhang, J. Zhou, F. Lv, K. Wang, F. Lin, H. Luo, J. Li, M. Tong, E. Wang and S. Guo, *Adv. Mater.*, 2021, **33**, 2102576.
11 R. Li and D. Wang, *Adv. Energy Mater.*, 2022, **12**, 2103564.
12 M. Dan, X. Zhang, C. Du, Z. Guo, J. Zhang and Z. Q. Liu, *Angew. Chem., Int. Ed.*, 2025, **64**, e202501531.
13 X. Jiang, C. Chen, J. Chen, S. Yu, W. Yu, L. Shen, B. Li, M. Zhou and H. Lin, *Sci. Total Environ.*, 2024, **912**, 169142.
14 M. K. Wong, J. J. Foo, J. Y. Loh and W. J. Ong, *Adv. Energy Mater.*, 2024, **14**, 2303281.
15 M. Dan, X. Zhang, Y. Yang, J. Yang, F. Wu, S. Zhao and Z.-Q. Liu, *Proc. Natl. Acad. Sci. U. S. A.*, 2024, **121**, e2318174121.
16 Y. T. He, X. C. Zhou, Y. F. Jia, H. T. Li, Y. Wang, Y. N. Liu and Q. Tan, *Small*, 2023, **19**, 2206477.
17 Z. Fan, H. Wan, H. Yu and J. Ge, *Chin. J. Catal.*, 2023, **54**, 56–87.
18 J. Herranz, F. Jaouen, M. Lefèvre, U. I. Kramm, E. Proietti, J.-P. Dodelet, P. Bogdanoff, S. Fiechter, I. Abs-Wurmbach, P. Bertrand, T. M. Arruda and S. Mukerjee, *J. Phys. Chem. C*, 2011, **115**, 16087–16097.
19 C. H. Choi, C. Baldizzone, J. P. Grote, A. K. Schuppert, F. Jaouen and K. J. J. Mayrhofer, *Angew. Chem., Int. Ed.*, 2015, **54**, 12753–12757.
20 X. Bai, Y. Wang, J. Y. Han, X. D. Niu and J. Q. Guan, *Appl. Catal., B*, 2023, **337**, 122966.
21 J. Li, M. Chen, D. A. Cullen, S. Hwang, M. Wang, B. Li, K. Liu, S. Karakalos, M. Lucero, H. Zhang, C. Lei, H. Xu, G. E. Sterbinsky, Z. Feng, D. Su, K. L. More, G. Wang, Z. Wang and G. Wu, *Nat. Catal.*, 2018, **1**, 935–945.
22 M. Liu, Y. Li, L. Yang, P. Zhao, J. Li, L. Tian, D. Cao and Z. Chen, *Angew. Chem., Int. Ed.*, 2025, **64**, e202505268.
23 Z. Wang, C. Li, Y. Liu, Y. Wu, S. Zhang and C. Deng, *J. Energy Chem.*, 2023, **83**, 264–274.
24 Y. Huang, Y. Zhao, D. Song, Y. Shi, H. Chen, B. Niu, D. Long and Y. Zhang, *Appl. Catal., B*, 2025, **374**, 125377.
25 W. Lu, Q. An, C. Wang, N. Gao, L. Huang, D. Gong, F. Sun, L. Sun, J. Pang, H. Zhang and L. Geng, *J. Mater. Sci. Technol.*, 2026, **255**, 118–133.
26 X. Chen, D.-D. Ma, B. Chen, K. Zhang, R. Zou, X.-T. Wu and Q.-L. Zhu, *Appl. Catal., B*, 2020, **267**, 118720.
27 X. Jin, M. Chang, H. Sun, C.-W. Chang, M. G. Sendeku, Y. Li, M. Wang, J. Fang, Y. Li, Q. Zhu, B. Li, J. Yu, Y. Liu, Z. Chang, G. Zhang, Z. Zhuang, L. Bai, Q. Ma, Z. Feng, W. Liu, J. Li and X. Sun, *J. Am. Chem. Soc.*, 2025, **147**, 2689–2698.
28 L. Qi, X. Bai, Y. Wang, Z. Duan, L. Li and J. Guan, *CCS Chem.*, 2025, **7**, 2508–2519.
29 Y.-J. Wang, B. He, D. Ma, R. Li, Y. Xie and J.-R. Li, *Chem. Eng. J.*, 2023, **467**, 143329.
30 J. Sun, T. Tang, S. Zhang, S. Chen, Y. Duan, X. Bai, X. Xu, X. Niu, Z. Wang and J. Guan, *Angew. Chem., Int. Ed.*, 2025, **64**, e202509063.
31 H. Meng, B. Wu, D. Zhang, X. Zhu, S. Luo, Y. You, K. Chen, J. Long, J. Zhu, L. Liu, S. Xi, T. Petit, D. Wang, X.-M. Zhang, Z. J. Xu and L. Mai, *Energy Environ. Sci.*, 2024, **17**, 704–716.
32 Y. Sheng, H. Zheng, J. Hou, W. Zhang, H. Chen, L. Nie, J. Zheng and Q. Lai, *Sustainable Energy Fuels*, 2023, **7**, 5557–5564.
33 T. Li, T. Lu, X. Li, L. Xu, Y. Zhang, Z. Tian, J. Yang, H. Pang, Y. Tang and J. Xue, *ACS Nano*, 2021, **15**, 20032–20041.
34 Y. Guo, Y. Xue and Z. Zhou, *Chem. Sci.*, 2024, **58**, 206–215.
35 P. Zhu, X. Xiong, X. Wang, C. Ye, J. Li, W. Sun, X. Sun, J. Jiang, Z. Zhuang, D. Wang and Y. Li, *Nano Lett.*, 2022, **22**, 9507–9515.
36 T. Tang, X. Xu, X. Bai, C. Hou, Z. Wang, T. Gan and J. Guan, *Angew. Chem., Int. Ed.*, 2025, **64**, e202503019.
37 C. Ye, L. Zhang and Y. Shen, *ACS Mater. Lett.*, 2024, **6**, 2858–2887.
38 H. Yu, L. Qi, Y. Hu, Y. Qu, P. Yan, T. T. Isimjan and X. Yang, *J. Colloid Interface Sci.*, 2021, **600**, 811–819.
39 H. Yang, X. Wang, S. Xia, S. Zhang, R. Zhang, X. Li, X. F. Yu, X. Zhang and L. Bai, *Adv. Energy Mater.*, 2023, **13**, 2302727.
40 X. Yan, D. Liu, P. Guo, Y. He, X. Wang, Z. Li, H. Pan, D. Sun, F. Fang and R. Wu, *Adv. Mater.*, 2023, **35**, 2210975.
41 Z. Zhang, Z. Xing, X. Luo, C. Cheng and X. Liu, *Nat. Commun.*, 2025, **16**, 921.
42 X. Wang, K. Li, D. Yang, X. Yang, M. Xiao, L. Zheng, W. Xing, C. Liu and J. Zhu, *Small*, 2024, **20**, 2310250.
43 Z. Tian, Y. Liang, K. Chen, J. Gao, Z. Lu, X. Hu, Y. Ding and Z. Wen, *Small*, 2024, **20**, 2310694.
44 X. Xu, T. Gan and J. Guan, *CCS Chem.*, 2025, DOI: **10.31635/ccschem.31025.202505566**.
45 C. Chen, J. Chai, M. Sun, T. Guo, J. Lin, Y. Zhou, Z. Sun, F. Zhang, L. Zhang, W. Chen and Y. Li, *Energy Environ. Sci.*, 2024, **17**, 2298–2308.
46 W. Xu, R. Zeng, M. Rebarchik, A. Posada-Borbón, H. Li, C. J. Pollock, M. Mavrikakis and H. D. Abruña, *J. Am. Chem. Soc.*, 2024, **146**, 2593–2603.
47 J. Kim and A. A. Gewirth, *J. Phys. Chem. B*, 2006, **110**, 2565–2571.
48 G. Yang, M. Fan, Q. Liang, X. He, W. Zhang and T. Asefa, *Angew. Chem., Int. Ed.*, 2024, **64**, e202421168.
49 W. Liu, Z. Liang, S. Jing, J. Zhong, N. Liu, B. Liao, Z. Song, Y. Huang, B. Yan, L. Gan, X. Xie, Y. Zou, X. Gui, H. B. Yang, D. Yu, Z. Zeng and G. Yang, *Angew. Chem., Int. Ed.*, 2025, **64**, e202503493.
50 Z. Duan and P. Xiao, *J. Phys. Chem. C*, 2021, **125**, 15243–15250.
51 Z. Duan and G. Henkelman, *J. Phys. Chem. C*, 2020, **124**, 12016–12023.
52 J. Liu, J. Q. Zhu, H. X. Xu and D. J. Cheng, *ACS Catal.*, 2024, **14**, 6952–6964.
53 Z. Liang, W. Liu, S. Jing, Y. Huang, B. Liao, X. Yan, Z. Qin, X. Gui, L. Gan, H. B. Yang, D. Yu, Z. Zeng and G. Yang, *ACS Nano*, 2025, **19**, 17863–17873.